Self-Reset Schemes for Magnetic Domain Wall-Based Neuron

DEBASIS DAS and XUANYAO FONG (Member, IEEE)

Department of Electrical and Computer Engineering, National University of Singapore, Singapore 117583

CORRESPONDING AUTHOR: D. DAS (eledd@nus.edu.sg)

ABSTRACT Spintronic artificial spiking neurons are promising due to their ability to closely mimic the leaky integrate-and-fire (LIF) dynamics of the biological LIF spiking neuron. However, the neuron needs to be reset after firing. Few of the spintronic neurons that have been proposed in the literature discuss the reset process in detail. In this article, we discuss the various schemes to achieve this reset in a magnetic domain wall (DW)-based spintronic neuron in which the position of the DW represents the membrane potential. In all the spintronic neurons studied, the neuron enters a refractory period and is reset when the DW reaches a particular position. We show that the self-reset operation in the neuron devices consumes energy that can vary from several pJ to a few fJ, which highlights the importance of the reset strategy in improving the energy efficiency of spintronic artificial spiking neurons.

INDEX TERMS Magnetic domains, magnetic domain wall (DW), micromagnetics, neuromorphics, spintronics.

I. INTRODUCTION

PROPOSALS for spintronics-based biological spiking leaky integrate-and-fire (LIF) neuron [1], [2] have demonstrated a promising pathway toward neuromorphic computing hardware that emulates the computations of the biological brain. In earlier works [3], [4], [5], [6], [7], [8], it has been demonstrated that the spintronics devices, such as magnetic tunnel junction (MTJ), can mimic the stochastic behavior of the neuron and synapses. After firing, the neuron enters a *refractory period* in which it is unresponsive to input spikes, and its membrane potential is reset. The reset mechanism for binary neurons made by MTJ has been demonstrated in the existing literature [5], [9]. However, apart from such binary operations, magnetic domain wall (DW)-based can also be used to mimic the neuronal [10], [11] as well as synaptic [12], [13], [14] operations. With the increasing demand for energy-efficient neuromorphic computing hardware, there is, hence, an urgent need to address the issue of resetting the membrane potential in spintronic neuronal devices, which, as we will show in this work, can consume significant amounts of energy if not carefully designed.

In this article, we consider magnetic DW-based LIF neurons where the membrane potential corresponds to the position of a magnetic domain in the device. Once the magnetic domain reaches the detector, it activates a certain mechanism based on the reset scheme, either by nucleating a new domain at the generator region or by sending a reset signal that sends the magnetic domain to its initial position. Based on the autoactivation of the reset mechanism upon firing, we propose various schemes to design a self-reset mechanism using monolayer as well as synthetic antiferromagnet (SAF) bilayer devices. The neurons studied in this work are implemented using a monolayer ferromagnet (FM) [15], [16] and an antiferromagnetically (AFM)-coupled bilayer system [2], [17]. Micromagnetic simulations were used to study the dynamics of the magnetic domain that acts as the membrane potential of the LIF neuron. The total energy required to complete the entire rest-to-fire-to-reset process is calculated so as to compare various self-reset schemes for the spintronic-based LIF neuron.

The rest of this article is organized as follows. In Section II, we describe various devices that we use to implement the working principle of an artificial neuron along with the mathematical framework used in our simulation. Detailed device operations and corresponding results for all the proposed devices are discussed in Section III, and Section IV concludes this article.

II. DEVICE CONCEPTS AND MODEL

In this section, we first describe the device structures used to implement the functionality of an LIF neuron in Section II-A. Thereafter, in Section II-B, we describe the micromagnetic
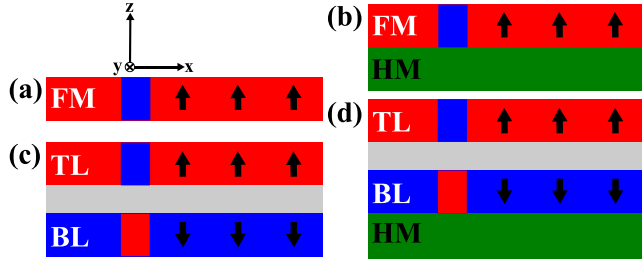
FIGURE 1. Side view of the schematic of (a) and (b) monolayer device and (c) and (d) bilayer device, along with the magnetic domain. Upward (downward) arrows show magnetization direction along the +(−)z-direction.

model for simulating the magnetization dynamics of the device.

A. DEVICE STRUCTURE

Structures, such as monolayer and AFM-coupled bilayer structures (shown in Fig. 1), were considered for possible implementations of self-resetting spintronic LIF neuron. The monolayer device consists of a single FM layer, as shown in Fig. 1(a) and (b), whereas in an SAF bilayer system, two FM layers—top layer (TL) and bottom layer (BL)—are separated by a thin nonmagnetic (NM) layer, as shown in Fig. 1(c) and (d). All the FM layers are assumed to have perpendicular magnetic anisotropy (PMA). In a bilayer system, the magnetization of TL and BL is coupled through an AFM exchange interaction, and due to PMA, the magnetization of these two layers is oriented along the +z- and −z-directions, respectively.

The position of the magnetic domain represents the membrane potential, and it can be driven either by spin-transfer torque (STT) or spin–orbit torque (SOT). STT is generated by injecting a spin-polarized current into FM in Fig. 1(a) and BL in Fig. 1(c), which induces a Zhang-Li torque [18] that moves the DW opposite to the direction of the current. Alternatively, injection of a charge current (along the +x-direction) into the heavy metal (HM) layer beneath the FM layer in Fig. 1(b) and BL in Fig. 1(d) gives rise to a +z-directed spin current (polarized along the y-direction), which is injected into the adjacent FM/BL layer [11] that moves the DW using SOT.

B. MICROMAGNETIC MODEL

The Hamiltonian for a magnetic layer is given as follows:

$$H^l = K_u^l \sum_i \left(1 - \left(\mathbf{m}_i^l \cdot \mathbf{z} \right)^2 \right) + H_{\text{dipole}}^l$$

$$+ A_{\text{intra}} \sum_{\langle i,j \rangle} \mathbf{m}_i^l \cdot \frac{\mathbf{m}_i^l - \mathbf{m}_j^l}{\Delta_{ij}} \quad (1)$$

where l represents the index of the magnetic layer in the device. $\mathbf{m}_i^l$ represents the local normalized magnetization vector, and $\langle i,j \rangle$ denotes the nearest neighbor interaction in layer l. The first term in (1) represents the energy for PMA, where K_u^l is the anisotropy constant for layer l. The second term represents the energy due to dipole–dipole interactions.

The third term represents the intralayer exchange interaction, where A_{intra} is the exchange stiffness constant, and Δ_{ij} is the discretization size between cell i and cell j. In the devices shown in Fig. 1(b) and (d), the HM attached to the magnetic layer may induce Dzyaloshinskii–Moriya interaction (DMI) with energy given by

$$H_{\text{DMI}} = \sum_{\langle i,j \rangle} \mathbf{D} \cdot \left(\mathbf{m}_i^l \times \mathbf{m}_j^l \right) \quad (2)$$

where $\mathbf{D}$ is the DM vector whose magnitude is denoted by D. In the bilayer system, there is also an additional energy due to interlayer AFM-coupled exchange interaction between BL and TL, which is given by

$$H_{\text{inter}} = \sigma \sum_k \frac{1 - \mathbf{m}_k^{\text{TL}} \cdot \mathbf{m}_k^{\text{BL}}}{\Delta_k} \quad (3)$$

where σ is the bilinear surface exchange coefficients between the two layers, and Δ_k is the discretization cell size in the direction from cell k of BL toward cell k of TL. Thus, the net Hamiltonian for the different systems considered in this work is given by

$$H^{\text{net}} = \begin{cases} H^{\text{FM}}, & \text{monolayer} \\ H^{\text{FM}} + H_{\text{DMI}}, & \text{monolayer} + \text{HM} \\ H^{\text{TL}} + H^{\text{BL}} + H_{\text{inter}}, & \text{bilayer} \\ H^{\text{TL}} + H^{\text{BL}} + H_{\text{inter}} + H_{\text{DMI}}, & \text{bilayer} + \text{HM} \end{cases} \quad (4)$$

which provides an effective magnetic field $\mathbf{H}_{\text{eff}}^l = -\partial H^{\text{net}}/\partial \mathbf{m}^l$ acting on layer l of the system.

The magnetization dynamics of the DW in a layer l is simulated by solving the Landau–Lifshitz–Gilbert–Slonczewski (LLGS) equation under the influence of $\mathbf{H}_{\text{eff}}^l$, given by

$$\frac{d\mathbf{m}^l}{dt} = -\gamma \left(\mathbf{m}^l \times \mathbf{H}_{\text{eff}}^l \right) + \alpha \left(\mathbf{m}^l \times \frac{d\mathbf{m}^l}{dt} \right) + \boldsymbol{\tau}^l \quad (5)$$

where $\gamma = 2.211 \times 10^5$ m/(A · s) is the gyromagnetic ratio, and α is the Gilbert damping factor. The first and the second terms in (5) are the precession and damping terms, respectively. $\boldsymbol{\tau}$ is the spin torque acting on layer l, which is Zhang-Li torque for the devices without the HM and SOT for the devices with the HM. Zhang-Li torque is given by

$$\boldsymbol{\tau}_{\text{ZL}} = -(\mathbf{u} \cdot \boldsymbol{\nabla}) \mathbf{m}^l + \beta_{\text{STT}} \mathbf{m}^l \times \left[(\mathbf{u} \cdot \boldsymbol{\nabla}) \mathbf{m}^l \right] \quad (6)$$

where $\mathbf{u} = (JPg\mu_B)/(2eM_S)\hat{i}$ is the velocity vector along the direction of electron motion. Here, J is the current density, P is the spin polarization, g is the Landé factor, μ_B is the Bohr magneton, e is the electronic charge, M_S is the saturation magnetization, and $\hat{i}$ is the unit vector along the x-direction denoting the direction of the electron flow. β_{STT} is a factor related to nonadiabatic STT.

Alternatively, SOT is given by

$$\boldsymbol{\tau}_{\text{SOT}} = -\gamma \beta_{\text{SOT}} \left[\epsilon \left(\mathbf{m}^l \times \mathbf{m}^l \times \mathbf{m}_p \right) + \epsilon' \left(\mathbf{m}^l \times \mathbf{m}_p \right) \right] \quad (7)$$

TABLE 1. Device simulation parameters.

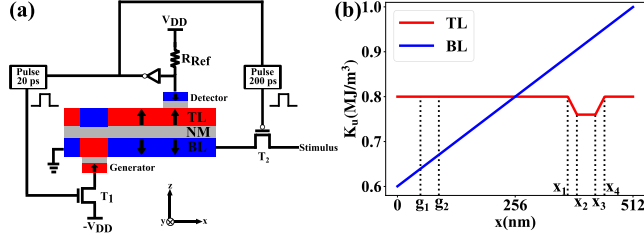| Parameters	Value
Saturation magnetization, M_s	580 kA/m
Gilbert damping factor, α	0.3
Spin polarization factor, P	0.4
PMA constant, K_u	0.8 MJ/m^3
Anisotropy gradient, ΔK_u	0.78125 GJ/m^4
Exchange stiffness constant, A_{intra}	15 pJ/m

FIGURE 2. (a) Schematic of the side view of the device along with the electrical connections from the detector to the generator. (b) K_u profile along the length of the device. K_u for TL at $x_1 = 370$ nm and $x_4 = 450$ nm is 0.8 MJ/m^3, whereas it is 0.76 MJ/m^3 at $x_2 = 390$ nm and $x_3 = 430$ nm. The detector spans from x_2 to x_3, whereas the generator spans from $g_1 = 50$ nm to $g_1 = 90$ nm.

where $\beta_{\text{SOT}} = \hbar J_{\text{HM}}/(\mu_0 e t_z M_S)$, $\hbar$ is reduced Planck's constant, J_{HM} is the charge current density injected to the HM, μ_0 is the free space permeability, e is the electronic charge, and t_z is the thickness of the magnetic layer above the HM. $\epsilon = P\Lambda^2/((\Lambda^2+1)+(\Lambda^2-1)(\mathbf{m}^l \cdot \mathbf{m}_p))$, where $\Lambda \geq 1$, and $\mathbf{m}_p$ is the direction of the spin polarization. ϵ' is the secondary spin-transfer term.

III. RESULT AND DISCUSSION

The object-oriented micromagnetic framework (OOMMF) was used to perform micromagnetic simulations of all devices in this work. The dimensions of all magnetic layers (FM, TL, and BL) are $512 \times 32 \times 1$ nm^3 discretized into 1-nm side cubes. Parameters used in the simulations are listed in Table 1.

The self-reset mechanism may be achieved using two methods: 1) by nucleating a second domain at the initial position without a reset current or 2) by injecting a reset current opposite to the stimulus current to return the magnetic domain to its initial position. One way to implement a device that achieves self-reset without a reset current is shown in Fig. 2(a). The device consists of an SAF formed by two AFM-coupled FMs layers that are separated by a thin NM layer. The MTJ-like structures on the left-hand side of the BL and the right-hand side of the TL form the *domain generator* and *detector*, respectively. The fixed layers of these MTJs also possess PMA, whereas BL and TL act as the free layers of the corresponding MTJs. A magnetic domain may be generated in BL by passing a current through the generator, which is controlled by the transistor, T_1. The widths of the detector and generator are identical to the width of the nanotrack (i.e., 32 nm). To emulate the leak functionality, the uniaxial anisotropy constant (K_u) of BL is designed to be described
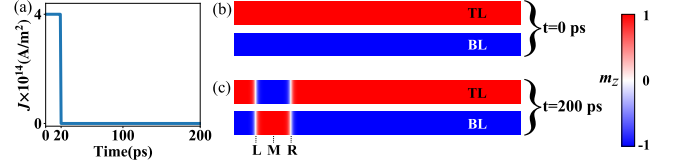

FIGURE 3. (a) 20-ps pulse is applied at the generator region to create the domain. A 2-D color plot for m_z on the xy plane for TL and BL at (b) 0 and (c) 200 ps.

by [1], [2], [19]

$$K_u(x) = K_u^c + \Delta K_u x. \tag{8}$$

This type of anisotropy gradient can be made by ion bombardment [20] during the fabrication of the device. The K_u profiles of BL and TL along the length of the device are shown in Fig. 2(b). Marks on the graph demarcate the locations of the generator and detector.

The neuron needs to be initialized first by injecting $+z$-directed spin-polarized current pulse locally in BL through the generator, as shown in Fig. 3(a), to nucleate the magnetic domains. This was achieved by applying a 20-ps current pulse of magnitude 4×10^{14} A/m^2, which flips the spin orientation of the local spins of the BL to the $+z$-direction. Since BL and TL are AFM-coupled, a $-z$-directed magnetic domain is created in the TL adjacent to the $-z$-directed magnetic domain in the BL. From Fig. 3, we observe that the nucleated magnetic domain is stable even after the removal of the current pulse. The 2-D color plots of m_z on the xy plane in TL and BL are shown in Fig. 3(b) and (c) for the time instances $t = 0$ ps (at the beginning of the pulse) and $t = 200$ ps, respectively. The calculation of the consumed energy can be obtained by the following [2], [21]:

$$E = \rho L A J^2 t_{\text{delay}} \tag{9}$$

where ρ is the resistivity of the material, L is the length of the device, A is the cross-sectional area through which the current flows, J is the current density, and t_{delay} is the time required to complete the operation. The energy consumed to nucleate the domains is ≈ 1.11 pJ. In Fig. 3(c), M, L, and R represent the position of the midpoint, left, and right walls of the magnetic domain, respectively.

The entire rest-to-fire-to-reset operation of the self-resetting neuron can be described in three steps. In the first step, the input stimulus is injected along the $-x$-direction to the BL in the form of a square current pulse train with 0.5-ns pulsewidth and 1-ns period, as shown in Fig. 4(a) (red curve). In the rest of this article, we assume the same pulsewidth and time period for the square current pulse train, applied to the various proposed neuron devices. Here, we assume the magnitude of the applied J is 4×10^{12} A/m^2. The induced STT during the high state of the current pulse pushes the DW along the $+x$-direction [18], [22], [23], whereas during the low state of the current pulse, the DW move in the opposite direction due to the anisotropy gradient [15] in BL. This is shown by the corresponding blue graph of the position of M
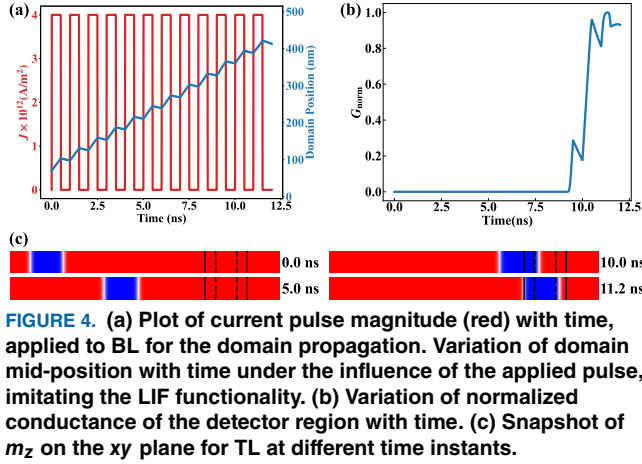
FIGURE 4. (a) Plot of current pulse magnitude (red) with time, applied to BL for the domain propagation. Variation of domain mid-position with time under the influence of the applied pulse, imitating the LIF functionality. **(b)** Variation of normalized conductance of the detector region with time. **(c)** Snapshot of m_z on the xy plane for TL at different time instants.

versus time in Fig. 4(a), which confirms that the device performs the leaky and integration functionality of a biological neuron. After sufficient current spikes, the magnetic domain enters the detector region and becomes pinned due to the K_u well in TL [refer to Fig. 2(b)]. The energy consumed for the continuous spike integration in Fig. 4(a) is $\approx$0.4 pJ. As shown in Fig. 2(a), the magnetization of the fixed layer of the detector is pinned in the $-z$-direction. When the magnetic domain in TL reaches under the detector, the detector MTJ becomes the parallel state and causes the conductance across it to increase. The conductance, G, of this MTJ is calculated using

$$G = G_0 \sum_i \frac{1 + P^2 \cos \theta_i}{1 + P^2} \qquad (10)$$

where G_0 is the conductance when all the spins of the free and fixed layer of the detector unit are perfectly parallel to each other, P is the spin polarization, and θ_i is the angle between the magnetization of the ith cell of the fixed layer of the detector and the corresponding region of TL. Fig. 4(b) graphs the change of normalized conductance, $G_{norm} = (G - G_{min})/(G_{max} - G_{min})$, with time as the magnetic domain moves. When the domain is not in the detector region, $G_{norm} = 0$. As the domain enters the detector region, G_{norm} increases and reaches a maximum value at 11.2 ns. A few snapshots of m_z on the xy plane for TL at different time instants are shown in Fig. 4(c). The black solid (dashed) vertical lines are drawn at $x = 370$ nm and $x = 450$ nm ($x = 390$ nm and $x = 430$ nm), respectively, to mark the locations where K_u is changing in the TL. Similar magnetic domains but with opposite polarization are found in the BL (not shown in the figure).

When the magnetic domain is pinned in the detector, the neuron fires, and a two-step reset process is triggered by activating two voltage pulses for 20 and 200 ps, respectively, as shown in Fig. 2(a). One purpose of these pulses is to prevent input stimulus from being injected into BL, thereby achieving the refractory behavior of the LIF neuron. The other purpose is to perform the first step in the reset process by first nucleating a new magnetic domain in the generator.
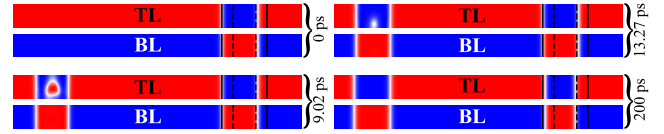

FIGURE 5. Snapshot of m_z on the xy plane for TL and BL, respectively, at different time instants.
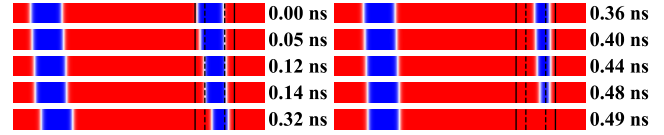

FIGURE 6. Snapshot of m_z on the xy plane for TL at different time instants.

The magnetic domain in the detector region is eliminated during the second step of the reset process, which we discuss later.

The 20-ps pulse turns on the transistor T_1, causing spin-polarized current to flow through the generator. Alternatively, the 200-ps pulse deactivates the transistor T_2, ensuring no input stimulus is applied to the BL, and the neuron enters into the refractory period during this time. The spin-polarized current through T_1 nucleates a pair of magnetic domains at TL and BL in the generator region just like in the initialization process described earlier. This process is depicted through the snapshots of m_z on the xy plane at different time instants shown in Fig. 5. At $t = 0$ ps, there are only magnetic domains in TL and BL under the detector region. As soon as the spin-polarized current enters the BL through the generator, local spins in that region of the BL start to flip—the corresponding spins in TL also flip due to the AFM exchange coupling. After some time, magnetic domains can be found in the generator and detector regions in the TL and BL, as shown in Fig. 5 for $t = 200$ ps.

In the final step of the two-step reset process, a single current pulse such as the one in Fig. 4(a) is applied to BL to eliminate the magnetic domain in the detector. This current exerts torque on both domains in the detector and the generator regions. Due to the finite gradient of K_u from $x = 430$ nm to $x = 450$ nm in TL, the right-most DW of TL in the detector region encounters an energy barrier that exerts a $-x$-directed force on the DW and prevents it from exiting the detector region toward the right. At the same time, the leftmost DW of TL in the detector region experiences no such force and is pushed to the right. Over time, magnetic domains in TL and BL under the detector are squeezed until they are annihilated completely. The process of annihilating the magnetic domains in the detector is depicted in Fig. 6 through the snapshots of m_z on the xy plane at different time instants. Thus, our simulation results confirm that the SAF-based LIF neuron device has the LIF behavior and with the desired self-reset behavior during the refractory period. For the entire rest-to-fire-to-reset operation, the neuron consumes $\approx$1.5 pJ of energy.

Alternatively, the reset operation in the neuron may be achieved by moving the magnetic domain from the detector
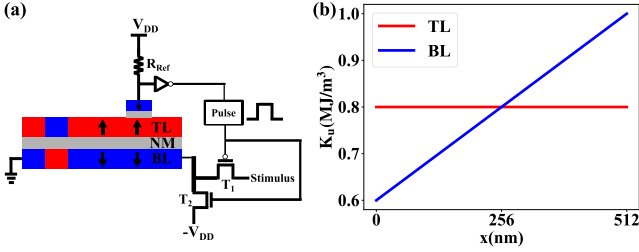
FIGURE 7. (a) Schematics of the bilayer device along with reset circuitry. (b) K_u profile along the length of the device.
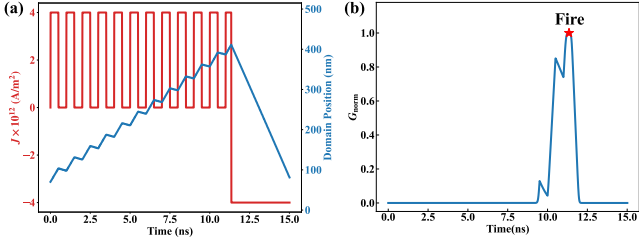

FIGURE 8. (a) Plot of current pulse train as the input stimulus injected to the device, along with the reset current after the neuron fires. (b) Variation of the normalized conductance of the detector region with time.

back to the generator. This is achieved by applying a reset current opposite to the stimulus after the neuron fires. A neuron with this method of self-reset may be implemented using an SAF bilayer device without a K_u well in TL. A schematic of the neuron device with the reset circuitry is shown in Fig. 7(a). An anisotropy gradient in the BL is used to implement the leaky behavior in the neuron. Unlike the previous bilayer device, there is no pinning site in TL (see Fig. 7). As an initial condition, consider a similar magnetic domain position, as shown in Fig. 3(c). The initial magnetic domain can be nucleated by attaching a generator similar to the previous device, which we do not include in the schematic for convenience. The position of this magnetic domain represents the membrane potential of the neuron.

To validate the integration functionality, the square pulse train in Fig. 8(a) (red curve) is applied to BL via the transistor T_1. An MTJ-like detector is placed at the right-hand side of the TL, which is connected to a voltage divider circuit via resistance R_{Ref}. The magnetic domain moves in the $+x$-direction whenever the magnitude of current is nonzero. When the current is zero, the magnetic domain moves in the $-x$-direction due to K_u gradient in BL, which emulates the leak functionality. The variation of the mid-position of the magnetic domain, M, versus time is shown in Fig. 8(a) (blue plot), which confirms the integrate and leak functionality of the neuron device. The magnetic domain takes ≈ 11.35 ns to reach the detector, which requires an energy of 378 fJ. Fig. 8(b) plots the normalized conductance of the detector region, G_{norm}, versus time. When the domain is outside of the detector region, G_{norm} is low. As the domain enters the detector region, G_{norm} starts to rise and reaches a maximum at 11.35 ns. Thereafter, the neuron fires, as shown in Fig. 8(b) (red asterisk).
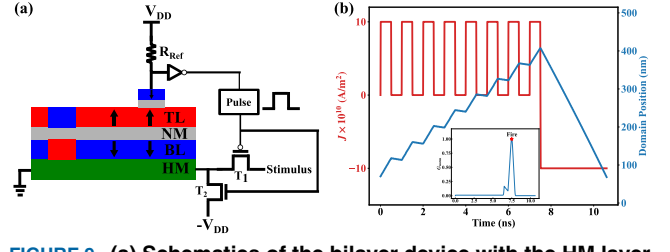

FIGURE 9. (a) Schematics of the bilayer device with the HM layer attached to the BL, along with reset circuitry. (b) Plot of the input stimulus in the form of current pulse train that is injected to the HM, along with the reset current after the neuron fires (red), and the corresponding domain position (blue). Inset: time variation of normalized conductance in the detector region.

When the neuron fires, the voltage divider circuit triggers a pulse generator circuit to generate a 3.66-ns voltage pulse, which deactivates the transistor T_1 shown in Fig. 7(a). This blocks any input stimulus, which means the neuron enters the refractory period. The pulse is also given to the transistor T_2 shown in Fig. 7(a), which allows a reset current of magnitude 4×10^{12} A/m^2 to flow along the $+x$-direction to move the domain back to its initial position, thus resetting the neuron. The energy consumed by the reset current is 260 fJ. Thus, for the entire rest-to-fire-to-reset operation, the neuron consumes ≈ 638 fJ of energy.

The neuron devices presented thus far utilize STT for DW motion and requires pJ level of energy consumption for the entire rest-to-fire-to-reset operation. The energy consumption may be further reduced if the charge current required is reduced. This may be achieved using SOT generated by an HM layer that is adjacent to the FM layer [2]. Let us now consider neuron devices that utilize SOT for magnetic domain motion.

The schematic of a neuron device that uses SOT is shown in Fig. 9(a), where the input stimulus is injected via transistor T_1, which is controlled by a pulse generator. Note that the device structure is similar to that in Fig. 7(a) except for the HM layer that is attached beneath the BL. The leaky behavior is achieved by the anisotropy gradient shown in Fig. 7(b) just like in the previous neuron device. Assume that the initial positions of the magnetic domains are similar to the devices described earlier. When the magnetic domain is not underneath the detector region, the output of the pulse generator is at 0 V, which keeps T_1 on and allows the input spikes to enter the device. Input spikes are applied as the square pulse train shown in Fig. 9(b) (red curve). As SOT devices are able to operate at lower current density [24], [25], we reduce the magnitude of the applied J to 10×10^{10} A/m^2. This charge current passes through the HM, which generates a vertical spin current that exerts SOT on the local magnetization in BL. The input stimulus moves the magnetic domain toward the detector region as shown by the plot of domain position versus time (blue graph) in Fig. 9(b). The results confirm the integrate and leaky behavior of the neuron. From the results, the magnetic domain requires 7.5 ns to reach the detector
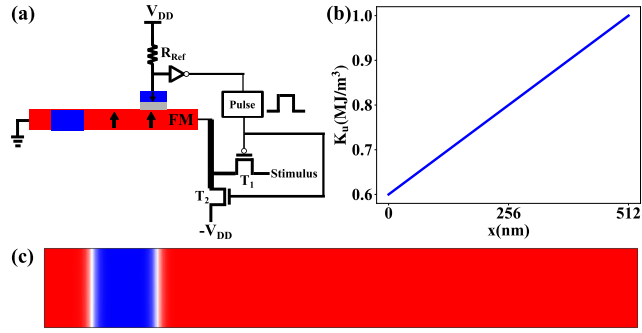
FIGURE 10. (a) Schematics of the monolayer device along with reset circuitry. (b) K_U profile along the length of the device. (c) Snapshot of m_z on the xy plane for the FM layer that is used as the initial magnetization profile for the monolayer neuron device.
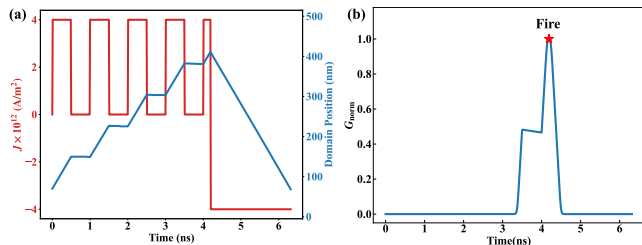

FIGURE 11. (a) Plot of the current pulse train as the input stimulus injected to the FM layer, along with the reset current after the neuron fires. (b) Variation of the normalized conductance of the detector region with time.
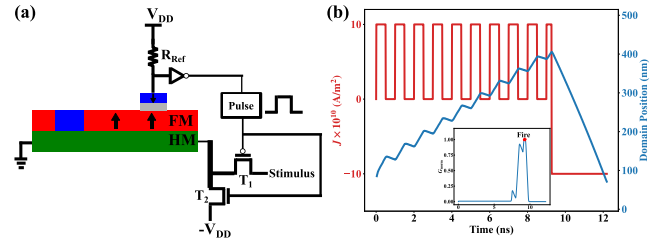

FIGURE 12. (a) Schematic of the monolayer device where an HM layer is attached to the FM, along with the reset circuitry. (b) Plot of the current pulse train as the input stimulus is injected into the HM layer, along with the reset current after the neuron fires shown by the red plot, and variation of the magnetic domain position due to this current is shown in blue curve. Inset: time variation of normalized conductance in the detector region.

from rest, and the energy consumed during the process is ≈ 0.65 fJ.

Once the magnetic domain reaches the detector, the neuron fires. The change in conductance in the detector region, G_{norm}, versus time is shown in Fig. 9(b) (inset), where the red asterisk denotes the moment the neuron fires. When this happens, the pulse generator is activated to output a 3.1-ns square pulse of magnitude 10×10^{10} A/m^2, as shown in Fig. 9(b). This pulse deactivates T_1 resulting in the neuron entering into the refractory period. Simultaneously, the transistor T_2 is activated, and a reset current passes through the device. This reset current returns the magnetic domains to their initial positions. The energy consumed by this reset process is ≈ 0.5 fJ. Thus, the total energy consumed by this device for the entire rest-to-fire-to-reset operation is 1.15 fJ.

Apart from the bilayer devices, the neuronal operation can also be achieved in the monolayer devices. Consider the monolayer device shown in Fig. 10(a). Similar to the previous devices, an anisotropy gradient along the length of the device shown in Fig. 10(b) may be used to achieve the leaky behavior. An MTJ-like detector is placed on the right-hand side of the device. A snapshot of m_z on the xy plane is shown in Fig. 10(c), showing the initial magnetization for the monolayer neuron device.

To validate the neuronal operation of the device, a square pulse train of magnitude 4×10^{12} A/m^2, shown in Fig. 11(a), is given as input stimulus to the device. From the plot of the domain position versus time (blue curve), it may be

observed that the magnetic domain moves toward and enters the detector after ≈ 4.19 ns. The normalized conductance of the detector region versus time is shown in 11(b), where the firing event is marked by the red asterisk. The energy consumed is ≈ 0.15 pJ. When the magnetic domain reaches the detector, the neuron fires by generating a voltage spike at the voltage divider circuit. This activates the pulse generator that generates a 2.12-ns square pulse of magnitude 4×10^{12} A/m^2 to deactivate transistor T_1 and activate transistor T_2. Deactivating transistor T_1 prevents input stimulus from affecting the device, which emulates the refractory period of the neuron. Activating transistor T_2 allows a reset current to reset the magnetic domain from the detector back to the initial position. Our results show that 2.12-ns delay is needed to reset the neuron; 0.15 pJ of energy is consumed during the reset process. Thus, the leaky-integrate-and-fire operation of the device is validated, and the total energy consumed for the entire rest-to-fire-to-reset operation for this monolayer device is about 0.3 pJ.

Similarly, the energy consumed by the monolayer device may be reduced by attaching an HM layer beneath the FM layer. The schematic of the device along with the reset circuitry is shown in Fig. 12(a). To validate the neuronal behavior of the device, consider the initial magnetization for this device to be as shown in Fig. 10(c). Input stimulus is applied to HM in the form of a square pulse train of magnitude 10×10^{10} A/m^2, shown in Fig. 12(b) (red curve). Our simulation results show that it takes 9.26 ns for the magnetic domain to move from its initial position to the detector region, as shown in Fig. 12(b) (blue curve), which plots the position of the magnetic domain versus time. The energy consumed during this process is ≈ 0.779 fJ. The graph of normalized conductance of the detector region versus time is shown in Fig. 12(b). Once the domain reaches the detector, the neuron fires and triggers the reset process, which is similar to that for the previous device. Our results indicate that the reset process takes 2.92 ns and consumes ≈ 0.47 fJ of energy. Thus, the total energy consumption for the entire rest-to-fire-to-reset operation is ≈ 1.25 fJ.

A comparison of the spintronic neurons studied in this work is shown in Table 2. These results show that SOT is

TABLE 2. Device simulation results.

Device	Spin-torque	Entire Operation Time	Consumed Energy
Bilayer with pinning site	STT	12 ns	1.5 pJ
Bilayer without pinning site	STT	15 ns	0.638 pJ
Bilayer+HM without pinning site	SOT	10.6 ns	1.15 fJ
Monolayer without pinning site	STT	6.31 ns	0.3 pJ
Monolayer+HM without pinning site	SOT	12.18 ns	1.25 fJ

a promising approach to reduce the total energy consumption of the spintronic neuron. Moreover, the method of returning the magnetic domain from the detector to the initial position remains the most energy efficient approach due to relatively the large voltage and current needed to nucleate a new magnetic domain in the generator. Furthermore, although the energy consumed for rest-to-fire operation can be in the sub-fJ regime, the energy consumed for the reset operation can be comparable. This further motivates the need to design novel schemes that can further reduce the energy consumed by the rest process.

We believe that there remains a range of values for J for the successful operation of these proposed devices, and it also affects the choice of reset timing. Obtaining the range needs a rigorous simulation for various values of J, which is beyond the scope of this work. Process variations are also worth investigating, as they provide an allowed range of parameter values for the successful operation of the proposed neuron devices. This also needs a rigorous simulation with the variation of different parameter values over a broad range. In this work, we intend to demonstrate various reset schemes for the neurons and compare the energy consumption between those schemes. Thus, we omit the parameter variations in this work and left as future work to pursue.

IV. CONCLUSION

In summary, several spintronic neuronal device concepts that have the ability to self-reset based on monolayer and SAF-coupled bilayer systems were investigated. Two methods of self-reset were studied to analyze their energy efficiency. In one method, the magnetic domain representing the membrane potential of the neuron is nucleated at the reset position, while the previous magnetic domain is annihilated. In the second method, a reset current is utilized to return the magnetic domain to its initial position after the neuron fires. Among schemes that were investigated, the devices utilizing SOT consume lesser energy. Furthermore, among the devices using SOT, the bilayer device may achieve 8% lower energy consumption than the monolayer device.

REFERENCES

[1] S. Li, W. Kang, Y. Huang, X. Zhang, Y. Zhou, and W. Zhao, "Magnetic skyrmion-based artificial neuron device," *Nanotechnology*, vol. 28, no. 31, Aug. 2017, Art. no. 31LT01.

[2] D. Das, Y. Cen, J. Wang, and X. Fong, "Bilayer-skyrmion based design of neuron and synapse for spiking neural network," 2022, *arXiv:2203.02171*.

[3] A. Sengupta, P. Panda, P. Wijesinghe, Y. Kim, and K. Roy, "Magnetic tunnel junction mimics stochastic cortical spiking neurons," *Sci. Rep.*, vol. 6, no. 1, pp. 1–8, Sep. 2016.

[4] D. Zhang, L. Zeng, Y. Zhang, W. Zhao, and J. O. Klein, "Stochastic spintronic device based synapses and spiking neurons for neuromorphic computation," in *Proc. IEEE/ACM Int. Symp. Nanosc. Archit. (NANOARCH)*, Jul. 2016, pp. 173–178.

[5] G. Srinivasan, A. Sengupta, and K. Roy, "Magnetic tunnel junction based long-term short-term stochastic synapse for a spiking neural network with on-chip STDP learning," *Sci. Rep.*, vol. 6, no. 1, pp. 1–13, Jul. 2016.

[6] C. M. Liyanagedera, A. Sengupta, A. Jaiswal, and K. Roy, "Stochastic spiking neural networks enabled by magnetic tunnel junctions: From non-telegraphic to telegraphic switching regimes," *Phys. Rev. A, Gen. Phys.*, vol. 8, no. 6, Dec. 2017, Art. no. 064017.

[7] A. Jaiswal, A. Agrawal, I. Chakraborty, D. Roy, and K. Roy, "On robustness of spin-orbit-torque based stochastic sigmoid neurons for spiking neural networks," in *Proc. Int. Joint Conf. Neural Netw. (IJCNN)*, Jul. 2019, pp. 1–6.

[8] J. Grollier, D. Querlioz, K. Y. Camsari, K. Everschor-Sitte, S. Fukami, and M. D. Stiles, "Neuromorphic spintronics," *Nature Electron.*, vol. 3, no. 7, pp. 360–370, Mar. 2020.

[9] G. Srinivasan, A. Sengupta, and K. Roy, "Magnetic tunnel junction enabled all-spin stochastic spiking neural network," in *Proc. Design, Autom. Test Eur. Conf. Exhib. (DATE)*, Mar. 2017, pp. 530–535.

[10] N. Hassan et al., "Magnetic domain wall neuron with lateral inhibition," *J. Appl. Phys.*, vol. 124, no. 15, Oct. 2018, Art. no. 152127.

[11] A. Sengupta, Y. Shim, and K. Roy, "Proposal for an all-spin artificial neural network: Emulating neural and synaptic functionalities through domain wall motion in ferromagnets," *IEEE Trans. Biomed. Circuits Syst.*, vol. 10, no. 6, pp. 1152–1160, May 2016.

[12] R. Zand, K. Y. Camsari, S. D. Pyle, I. Ahmed, C. H. Kim, and R. F. DeMara, "Low-energy deep belief networks using intrinsic sigmoidal spintronic-based probabilistic neurons," in *Proc. Great Lakes Symp. (VLSI)*, May 2018, pp. 15–20.

[13] A. Sengupta and K. Roy, "Encoding neural and synaptic functionalities in electron spin: A pathway to efficient neuromorphic computing," *Appl. Phys. Rev.*, vol. 4, no. 4, Dec. 2017, Art. no. 041105.

[14] A. Sengupta and K. Roy, "Neuromorphic computing enabled by physics of electron spins: Prospects and perspectives," *Appl. Phys. Exp.*, vol. 11, no. 3, Mar. 2018, Art. no. 030101.

[15] W. H. Brigner et al., "Graded-anisotropy-induced magnetic domain wall drift for an artificial spintronic leaky integrate-and-fire neuron," *IEEE J. Explor. Solid-State Computat. Devices Circuits*, vol. 5, no. 1, pp. 19–24, Jun. 2019.

[16] W. L. W. Mah, D. Kumar, T. Jin, and S. N. Piramanayagam, "Domain wall dynamics in (Co/Ni)n nanowire with anisotropy energy gradient for neuromorphic computing applications," *J. Magn. Magn. Mater.*, vol. 537, Nov. 2021, Art. no. 168131.

[17] X. Zhang, Y. Zhou, and M. Ezawa, "Magnetic bilayer-skyrmions without skyrmion Hall effect," *Nature Commun.*, vol. 7, no. 10293, pp. 1–7, Jan. 2016.

[18] S. Zhang and Z. Li, "Roles of nonequilibrium conduction electrons on the magnetization dynamics of ferromagnets," *Phys. Rev. Lett.*, vol. 93, no. 12, Sep. 2004, Art. no. 127204.

[19] D. Das, B. Muralidharan, and A. Tulapurkar, "Skyrmion based spin-torque nano-oscillator," *J. Magn. Magn. Mater.*, vol. 491, Dec. 2019, Art. no. 165608.

[20] M. Matczak et al., "Tailoring magnetic anisotropy gradients by ion bombardment for domain wall positioning in magnetic multilayers with perpendicular anisotropy," *Nanosc. Res. Lett.*, vol. 9, no. 1, pp. 1–7, Dec. 2014.

[21] T. Bhattacharya, S. Li, Y. Huang, W. Kang, W. Zhao, and M. Suri, "Low-power (1T1N) skyrmionic synapses for spiking neuromorphic systems," *IEEE Access*, vol. 7, pp. 5034–5044, 2019.

[22] A. Thiaville, Y. Nakatani, J. Miltat, and Y. Suzuki, "Micromagnetic understanding of current-driven domain wall motion in patterned nanowires," *EPL Europhys. Lett.*, vol. 69, no. 6, p. 990, Feb. 2005.

[23] S. S. P. Parkin, M. Hayashi, and L. Thomas, "Magnetic domain-wall racetrack memory," *Science*, vol. 320, no. 5873, pp. 190–194, 2008.

[24] A. V. Khvalkovskiy et al., "Matching domain-wall configuration and spin-orbit torques for efficient domain-wall motion," *Phys. Rev. B, Condens. Matter*, vol. 87, no. 2, Jan. 2013, Art. no. 020402.

[25] J. Chureemart, S. Sampan-a-pai, S. Boonchui, R. W. Chantrell, and P. Chureemart, "Current-induced domain wall motion: Comparison of STT and SHE," *J. Magn. Magn. Mater.*, vol. 529, Jul. 2021, Art. no. 167838.